Electronic Supplementary Material (ESI) for Journal of Materials Chemistry C.

Supporting Information

Solution-processable Yb/Er 2D-layered Metallorganic Frameworks with high NIR-emission quantum yield

Flavia Artizzu,*[a] Matteo Atzori,*[b] Jing Liu,[a] Dimitrije Mara,[a] Kristof van Hecke[a] and Rik Van Deun[a]

[a] L^3-Luminescent Lanthanide Lab (F. Artizzu, J. Liu, D. Mara, R. Van Deun) and Xstruct (K. Van Hacke), Department of Chemistry, Ghent University, Krijgslaan 281-S3, B-9000, Ghent, Belgium

[b] National High Magnetic Fields Laboratory, UPR 3228 - CNRS, and Université Grenoble-Alpes, 25 Rue de Martyrs - F-38042 Grenoble, France

Corresponding authors:

F. Artizzu: flavia.artizzu@ugent.be

M. Atzori: matteo.atzori@lncmi.cnrs.fr

Crystallography

Table S1. Summary of X-ray crystallographic data for **1** and **3**.

	1	**2**	**3**
Empirical formula	$C_{31}H_{30}Cl_3N_3O_{17}S_5Yb_2$	$C_{31}H_{30}Cl_3N_3O_{17}S_5Yb_1Er_1$	$C_{33}H_{36}Cl_3N_3O_{18}S_6Er_2$
Formula weight	1407.44	1386.66	1503.88
Crystal size, mm	0.97 × 0.62 × 0.52	0.97 × 0.62 × 0.52	0.30 × 0.20 × 0.02
Crystal system	Triclinic	Triclinic	Tetragonal
Space group	*P-1*	*P-1*	*I4/m*
a, Å	9.4641(3)	9.4433(3)	19.7597(10)
b, Å	10.6052(3)	10.6073(3)	19.7597(10)
c, Å	13.0261(4)	13.0079(4)	14.6295(10)
α, deg.	75.531(3)	75.844(2)	90
β, deg.	79.202(3)	79.142(3)	90
γ, deg.	87.392(3)	87.177(2)	90
V, Å^3	1243.53(7)	1240.78(7)	5712.0(7)
Z	1	1	2
T, K	101(2)	102(2)	100(2)
ρ (calcd), Mg/m^3	1.878	1.856	1.623
μ, mm^{-1}	11.148	11.148	9.192
θ range, deg.	3.56–75.40	3.27–89.59	3.74–69.20
GooF	1.058	1.022	1.056
*R*1	0.0565	0.0595	0.1255
*wR*2	0.1594	0.1627	0.1909

$R1 = \Sigma||Fo|-|Fc||/\Sigma|Fo|$, $wR2 = [\Sigma[w(Fo2-Fc2)2]/\Sigma[w(Fo2)2]]½$, $w = 1/[\sigma2(Fo2) + (aP)2 + bP]$, where $P = [\max(Fo2,0) + 2Fc2]/3$.

Full crystallographic data for the solved structures of compounds **1** and **2** have been deposited in the Cambridge Crystallographic Data Centre with CCDC numbers 1898800 (**1**), 1898801 (**2**) and 1916865 (**3**). They can be obtained free of charge via www.ccdc.cam.ac.uk/conts/retrieving.html.

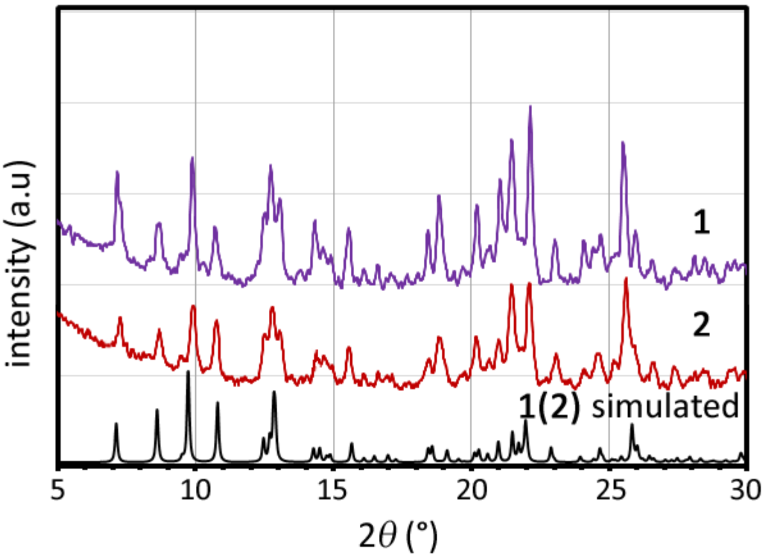

Figure S1. Powder-XRD patterns of **1** (purple) and **2**(red) compared to the simulated pattern for **1** (or **2**) from experimentally determined single-crystal XRD data.

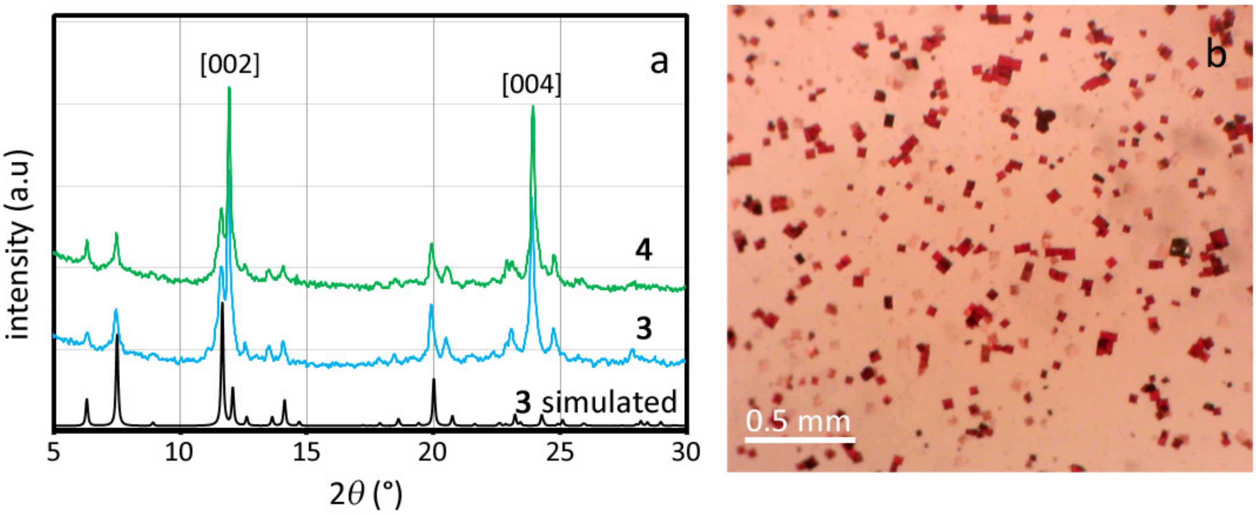

Figure S2. a. Powder-XRD patterns of **3** (blue) and **4** (green) compared to the simulated pattern for **3** from single-crystal XRD data in the 5°-30° 2θ range. The higher intensity of the peaks related to the crystallographic planes [002] and [004] is attributed to the preferential orientation of the cuboidal crystals on the flat surface of the pXRD sample holder. b. Optical microscope image of micrometer-sized crystals of **3** deposited by solvent thermal evaporation of a diluted (10^{-4} M) DMSO solution on a glass slide evidencing the preferential orientation of the crystals squared upper face corresponding to the unit cell *ab* plane.

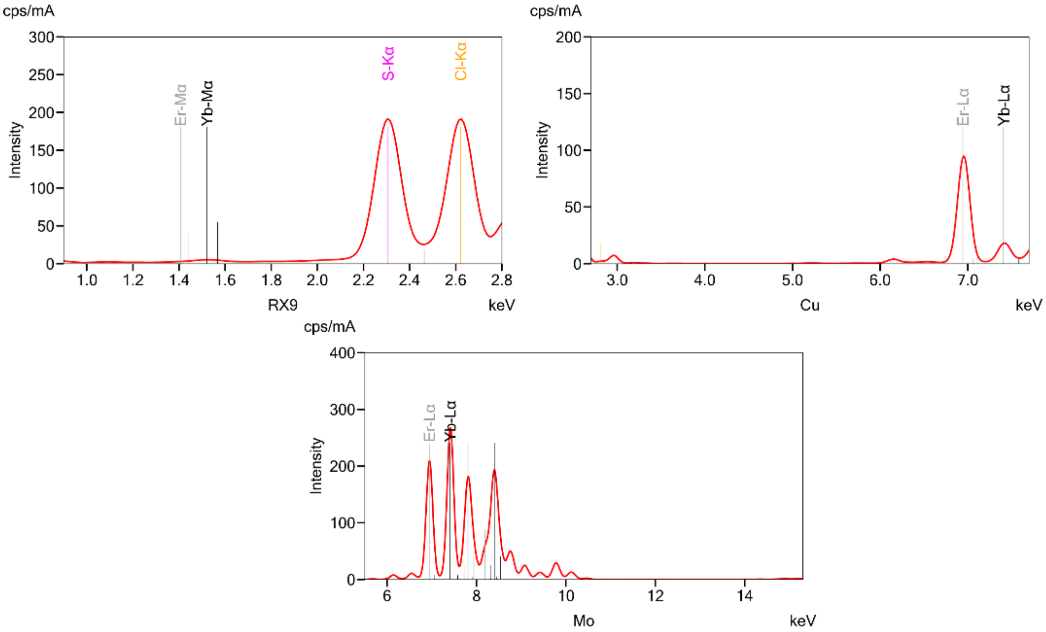

Figure S3. XRF spectra of a crystalline sample batch of **2**. Retrieved Yb:Er ratio was 1.001:1.000.

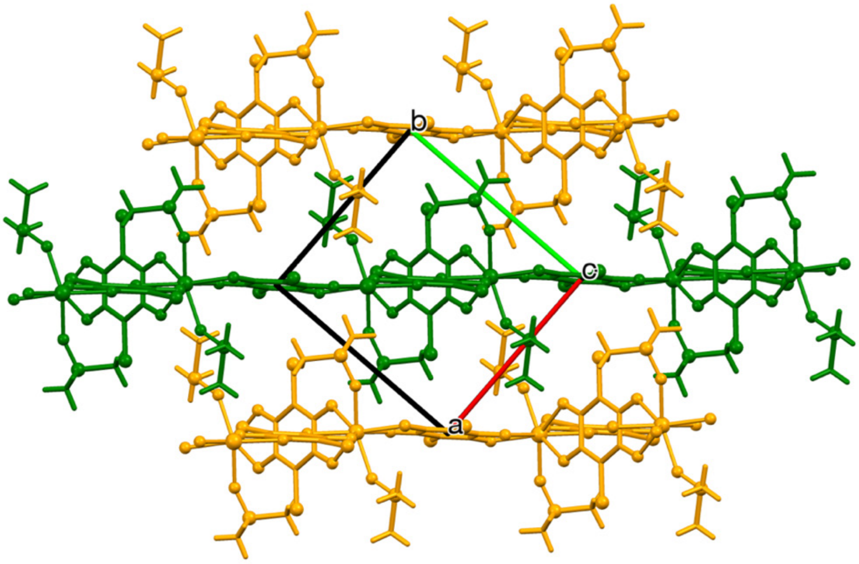

Figure S4 View of the crystal packing for **1-2** along the *c* axis.

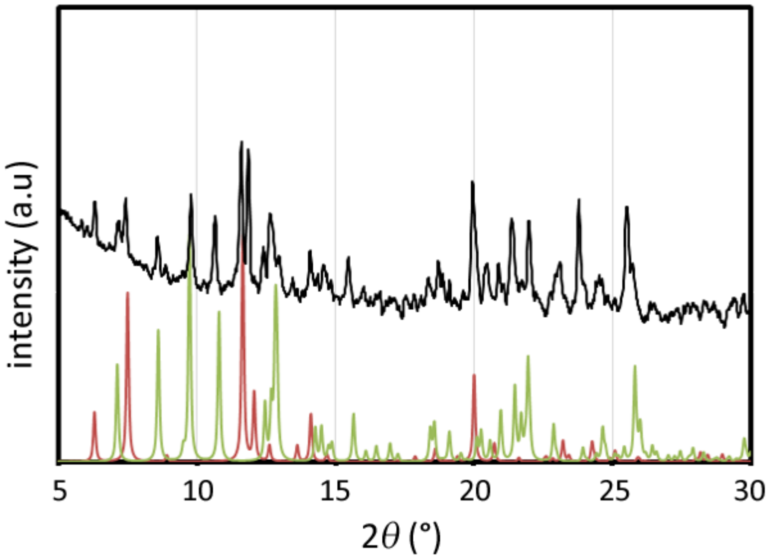

Figure S5. Powder-XRD patterns for the product obtained by using a Yb:Er = 0.5 stoichiometric ratio (black) compared to the simulated patterns of **1** (green) and **3** (red) from single-crystal XRD data in the 5°-30° 2θ range. The experimental diffractogram indicates the coexistence of the two crystal phases suggesting the existence of an upper limit for the inclusion of Er^{3+} ions in the structural arrangement templated by Yb^{3+}.

Sensitization mechanism and ligand-centered optical properties

Indirect photosensitization of the Ln emitter through ligand excitation is usually understood to occur through a two-step energy transfer mechanism, in which the excited ligand singlet state (S_1) first undergoes intersystem-crossing (ISC) to lower lying triplet states (T_1), triggered by the presence of the heavy Ln ion (heavy atom effect), then resonant energy transfer (RET) to the emitting metal follows.[S1] In the case of heterolanthanide systems, where the Ln ions have resonant energy levels, such as in the case of Yb^{3+} and Er^{3+}, metal-to-metal energy transfer can also occur as additional step in the mechanisms, as depicted in Figure S5.[S2]

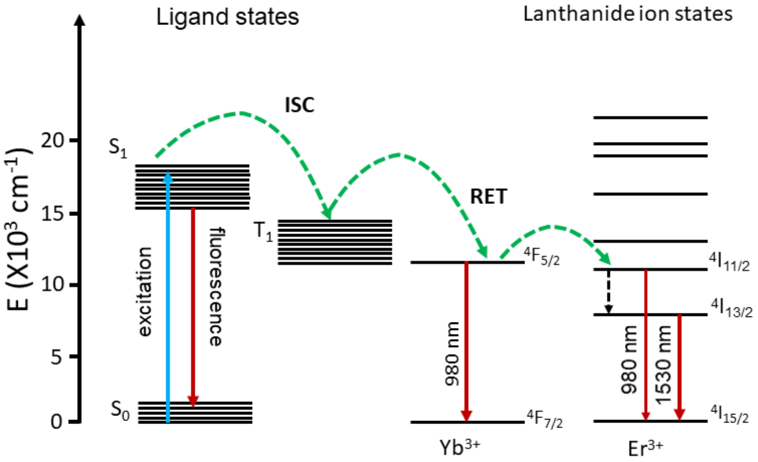

Figure S6. Jablonski diagram showing a scheme of the energy levels of the Ln chlorocyananilate derivatives and the photocycle leading to NIR emission consisting of a multi-step sequential mechanism. Solid and dashed arrows indicate radiative and non-radiative mechanisms, respectively.

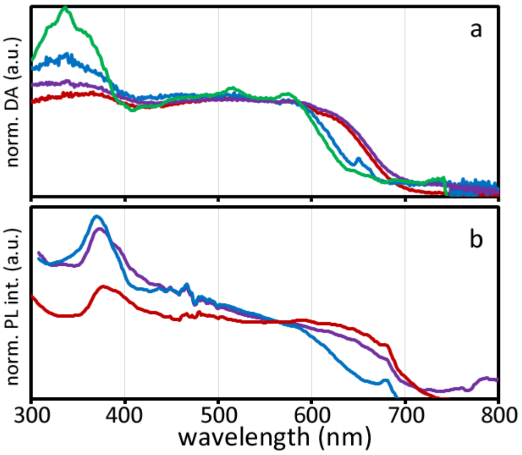

Figure S7. Diffuse absorbance (DA) (a) and excitation spectra of the NIR emission of **1** (λ_{em}=980 nm, purple), **2** (λ_{em}=980 nm, red) and **3** (λ_{em}=1530 nm, blue) in the crystalline state (b). The green curve in panel a) refers to **4**. Excitation spectra were corrected for the spectral contribution of the Xe lamp source. The small difference in the absorption spectral shape of **1-2** with respect to **3-4** is attributed to effects related to solid state interactions originating from the different structural arrangement of these compounds.

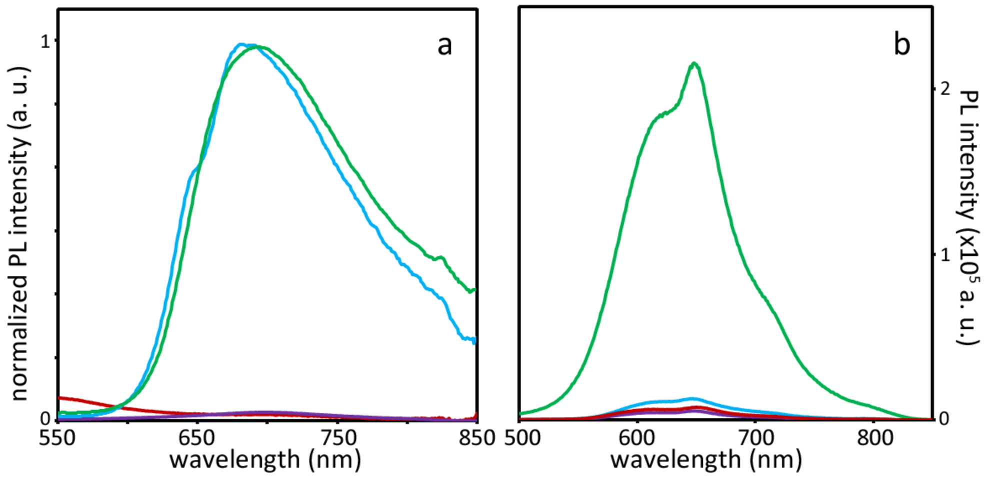

Figure S8. Steady-state emission spectra of the ClCNAn^{2-} ligand in the visible region for compounds **1-4** for bulk crystalline samples (a) and DMSO solutions (b). Color codes: **1**, purple; **2**, red; **3**; blue; **4**, green. In the solid-state, only a weak residual emission was detected for **3** and the retrieved spectrum has been normalized to the intensity of that in **4**. Solution spectra were corrected for absorbed power at excitation wavelength and intensity ratios are to be considered quantitative.

Lanthanide-centered NIR optical properties

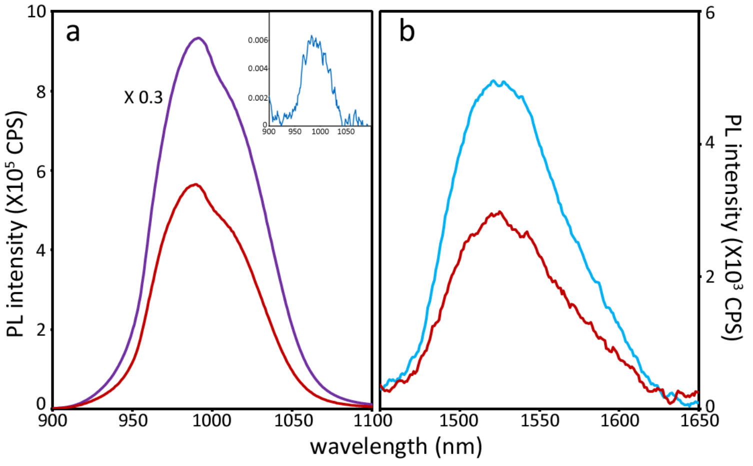

Figure S9. NIR steady-state emission spectra under 470 nm excitation of clear DMSO-*d*^{6} dispersions of **1-3**. a) Yb^{3+} emission at 980 nm in **1** (purple) and **2** (red) and b) Er^{3+} emission at 1530 nm in **3** (blue dots) and **2** (red). Er^{3+} emission at 980 nm in **3** ($^4I_{11/2}\rightarrow{}^4I_{15/2}$) is also reported in the inset of Figure S9a. All spectra have been corrected for absorbed power at excitation wavelength.

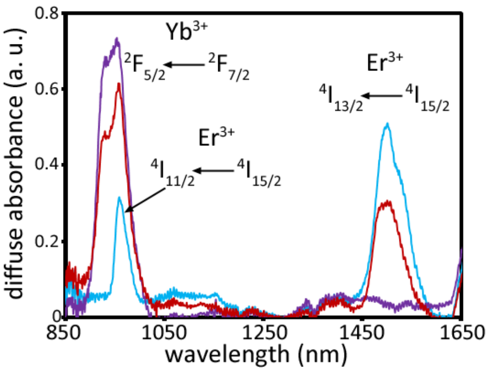

Figure S10. Diffuse absorbance (DA) spectra in the NIR region of **1** (purple), **2** (red) and **3** (blue) showing Yb^{3+} and Er^{3+} absorption lines. It is interesting to note the similarity of the absorption spectral fine structure to that observed in the PL lines (Figure 5), including the more resolved band of the Er^{3+} $^4I_{13/2}\leftrightarrow{}^4I_{15/2}$ transition in **3**, due to coordination symmetry effects in the different structures.

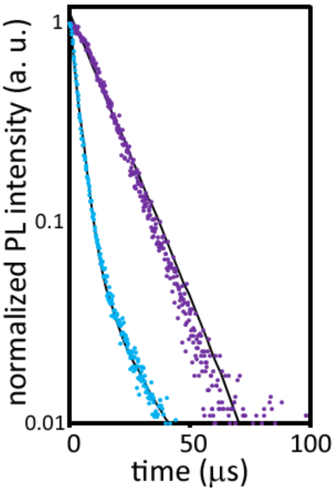

Figure S11. NIR decay dynamics under 470 nm excitation of clear DMSO dispersions of **1** and **3**: Yb^{3+} emission at 980 nm in **1** (purple dots) and Er^{3+} emission at 1530 nm in **3** (blue dots). Black solid lines represent the best fit to data.

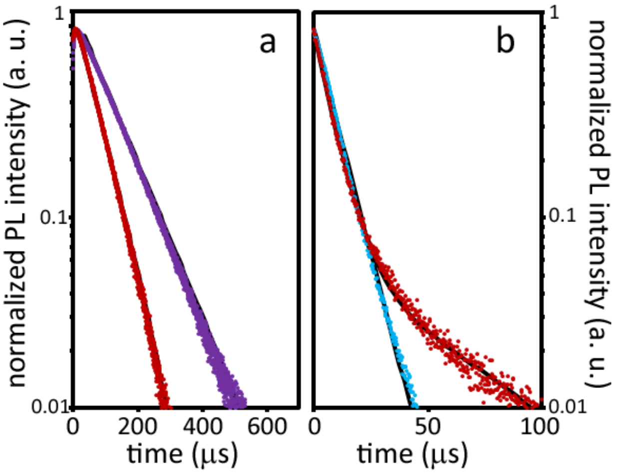

Figure S12. NIR decay dynamics under 470 nm excitation of clear DMSO-*d*^{6} dispersions of **1-3**. a) Yb^{3+} emission at 980 nm in **1** (purple dots) and **2** (red dots) and b) Er^{3+} emission at 1530 nm in **3** (blue dots) and **2** (red dots). Black solid lines represent the best fit to data.

Table S2. Main photophysical parameters in the NIR for **1-3**

	state	**τ Yb^{3+} $^2F_{5/2}\rightarrow{}^2F_{7/2}$ (μs)**	**τ Er^{3+} $^4I_{13/2}\rightarrow{}^4I_{15/2}$ (μs)**	**τ_{rad} (μs)**	**Φ_{Ln} (%)§**	**Φ^L_{Ln} (%)#**
1	crystals	17.73 ± 0.04	-		2.92 ± 0.05	2.5 ± 0.3
2	crystals	τ_1 = 12.49 ± 0.05 (38%); τ_2 = 1.39 ± 0.03 (62%)	10.17 ± 0.06		0.92 ± 0.05 (Yb^{3+}); 0.209 ± 0.003 (Er^{3+})	
3	crystals		9.74 ± 0.03		0.200 ± 0.003	0.16 ± 0.02
1	DMSO-d^6	108.66 ± 0.08	-	608 ± 1 ($^2F_{5/2}\rightarrow{}^2F_{7/2}$)	17.87 ± 0.05	15.6 ± 1.6
2	DMSO-d^6	65.15 ± 0.08	τ_1 = 7.49 ± 0.04 (94%); τ_2 = 63 ± 4 (6%)		10.72 ± 0.05 (Yb^{3+}); 0.222 ± 0.004 (Er^{3+})	
3	DMSO-d^6		9.10 ± 0.02	4860 ± 50 ($^4I_{13/2}\rightarrow{}^4I_{15/2}$)	0.187 ± 0.002	0.16 ± 0.02
1	DMSO	15.50 ± 0.09	-	608 ± 1 ($^2F_{5/2}\rightarrow{}^2F_{7/2}$)	2.55 ± 0.04	2.2 ± 0.3
3	DMSO		τ_1 = 3.39 ± 0.03 (92%); τ_2 = 16.3 ± 0.9 (8%)	4860 ± 50 ($^4I_{13/2}\rightarrow{}^4I_{15/2}$)	0.091 ± 0.003	0.08 ± 0.01
1	dropcasted film	15.37 ± 0.09	-	-	2.53 ± 0.05	2.2 ± 0.3
2	dropcasted film	τ_1 = 2.97± 0.05 (54%); τ_2 = 15.5 ± 0.2 (46%)	8.63 ± 0.03	-	1.43 ± 0.05 (Yb^{3+}); 0.178 ± 0.004 (Er^{3+})	
3	dropcasted film	-	τ_1 = 8.1 ± 0.1 (82%); τ_2 = 20.7 ± 0.9 (18%)	-	0.214 ± 0.003	0.18 ± 0.02

§ Φ_{Ln} are all calculated through τ_{rad} values for **1** and **3** in DMSO solution; # Relative Φ^L_{Ln} were measured for **1** and **3** in DMSO and DMSO-d^6. Values for bulk crystals and dropcasted films were determined using retrieved sensitization efficiency values (*vide infra*).

Radiative lifetime and NIR emission quantum yield

The lanthanide "natural" radiative lifetimes (i.e. the lifetimes in the absence of any quenching phenomena), τ_{rad}, have been experimentally determined from spectroscopic data (absorption cross-section, σ_{Ln}, Figure S12) through the Strickler-Berg equation:[S3]

$$\kappa_{\mathrm{rad}} = \tau_{\mathrm{rad}}^{-1} = 8\pi n^2 c \frac{2J+1}{2J'+1} \int \frac{\sigma_{\mathrm{Ln}}(\lambda)}{\lambda^4} d\lambda$$

where n is the refractive index of the medium (1.479 for DMSO), c is the speed of light in vacuum and J, J' refer to the ground and excited state respectively. τ_{rad} values of 685 (±1) µs and 4.86 (±0.10) ms are retrieved for Yb^{3+} and Er^{3+} in **1** and **3**, respectively. By reliably assuming that the lanthanide oscillator strength, which solely depends on the coordination environment, does not substantially change in analogous compounds in different phases, these values have been used to estimate all the intrinsic quantum yields Φ_{Ln} reported in Table S1.

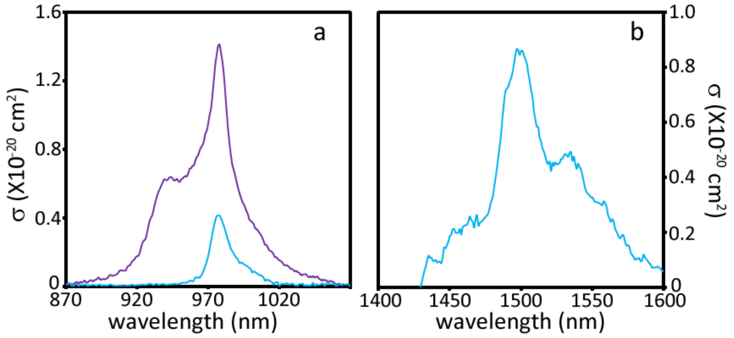

Figure S13. Absorption cross-section (σ) of lanthanide transitions in clear DMSO dispersions of **1** (purple) and **2** (blue): a) Yb^{3+} $^2F_{5/2} \leftarrow {}^2F_{7/2}$ and Er^{3+} $^4I_{11/2} \leftarrow {}^4I_{15/2}$ transitions; b) Er^{3+} $^4I_{13/2} \leftarrow {}^4I_{15/2}$ transition.

The determination of the absorption cross-section of the lanthanides transitions in the NIR was performed on highly concentrated (10^{-2} M) DMSO solutions to achieve a satisfactory signal-to-noise ratio and the baseline was manually subtracted, as described in detail in reference S2.

Total quantum yield and ligand-to-metal sensitization efficiency

Total quantum yields for **1** and **3** under ligand excitation at 470 nm were measured with the relative method as described in ref. S4 and according to the equation:

$$\Phi_{Ln}^{L} = \Phi_{st} \frac{I_{Ln}}{I_{st}} \frac{f_{st}}{f_{Ln}} \frac{n_{Ln}}{n_{st}}$$

where *Ln* and *st* indexes denote the investigated sample and a reference standard, *I* is the integrated corrected emission, *f* is the absorption factor at the excitation wavelength ($=1\text{-}10^{-A}$, where A is the absorbance) and *n* is the refractive index of the medium. $YbClQ_4$[S5] ($\Phi = 1.4 \cdot 10^{-2}$, $\lambda_{em} = 980$ nm) and $ErClQ_4$[S6] ($\Phi = 3.8 \cdot 10^{-2}$, $\lambda_{em} = 1540$ nm) (general formula $[LnCl(HClQ)_2(ClQ)_2]$, HClQ = 5,7-dichloro-8-quinolinol) in DMSO solution ($5 \cdot 10^{-4}$ M) were used as suitable references for **1** and **3**, respectively. Total quantum yield values were measured for solutions of **1** and **3** in deuterated and non-deuterated DMSO, as reported in Table S2. An error of ±10% is estimated on the retrieved values.

The ligand-to-metal sensitization efficiency η was then determined from the equation $\Phi^{L}_{Ln} = \eta\Phi_{Ln}$, yielding 0.87 ± 0.09 for **1** and 0.84 ± 0.08 for **3**. Deviations between independently determined values in DMSO and DMSO-*d*^{6} were within experimental error. These parameters were then used to evaluate the total quantum yield of solid state samples.

Yb-to-Er energy transfer

The efficiency of the Yb-to-Er energy transfer process η_{ET} can be retrieved from the observed time constants of Yb^{3+} emission in the presence (τ_{YbEr}) and in the absence of Er^{3+} (τ_{Yb}) in compounds **2** and **1**, respectively, according to the equations:

$$\tau_{ET} = \frac{1}{\kappa_{ET}} = \frac{1}{\frac{1}{\tau_{YbEr}} - \frac{1}{\tau_{Yb}}}$$

$$\eta_{ET} = \frac{1}{1 + \frac{\tau_{ET}}{\tau_D}}$$

where $\varkappa_{ET}$ and τ_{ET} are the rate and time constant of the energy transfer process, respectively.

Results for Yb-to-Er energy transfer in **2** in the bulk crystalline state, clear DMSO-d^6 dispersions and as dropcasted film are reported in Table S3. Since Yb^{3+} and Er^{3+} ions are randomly distributed across the infinite 2D-layered coordination network and metals sites are indistinguishable, we opted for using the average time constants (see Experimental Section) of bi-exponential Yb^{3+} decays without further discriminating the lifetime components and/or discussing the relative positioning of the donor ions with respect to the acceptors.

Table S3. Yb-to-Er energy transfer parameters

state	**$\varkappa_{ET}$ (μs^{-1})**	**η_{ET} (%)**
crystals	0.12	69
DMSO-d^6 dispersion	0.006	40
dropcasted film	0.05	44

Förster's energy transfer model

D = donor; A = acceptor

According to the Förster's model, the energy transfer rate constant $\varkappa_{ET}$ for a donor-acceptor pair can be written as:[S7]

$$\kappa_{ET} = \frac{1}{\tau_{ET}} = \frac{1}{\tau_D} \frac{9\kappa_j^2}{128\pi^5 n^4 R_{DA}} J = \frac{1}{\tau_D} \left(\frac{R_0}{R_{DA}}\right)^6$$

Where: R_{DA} is the donor-acceptor distance retrieved through structural data; R_0-is the Förster's radius; τ_D is the decay time constant of the donor in the absence of the acceptor, n is the refractive index of the medium (taken as 1.4772 for DMSO); $\varkappa_j^2$ is a dipole orientation factor, which depends on the relative orientation between the transition dipoles of the donor and the *j*th acceptor and *J* is the spectral overlap integral expressed as follows:

$$J = \int F_D(\lambda)\sigma_A(\lambda)\lambda^4 d\lambda$$

where $F_D(\lambda)$ represents the donor emission spectral density (nm^{-1}) normalized to unity, and $\sigma_A(\lambda)$ is the acceptor absorption cross-section (cm^2).

Since lanthanide ions are more rigorously behaving as quadrupoles rather than dipoles, a definite orientation of the emitting and accepting oscillators cannot be accurately established. Therefore, we take the average value $\kappa^2 = 2/3$, referred to a random spatial distribution of dipoles, as reliable value.

Compounds **1** and **3** were used to evaluate the spectral overlap integral, assuming that the oscillator strength of the two ions is the same in all the analogous compounds. Calculations yielded $J = 1.06 \cdot 10^5\ nm^6$. A graphical representation of the involved spectral overlap for the Yb-to-Er energy transfer is shown in Figure S14.

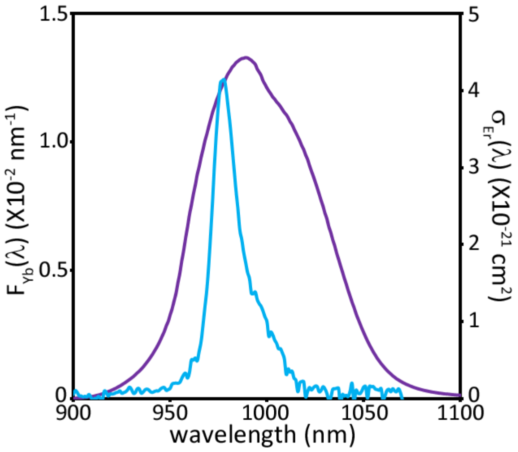

Figure S14. Overlap between the Yb^{3+} normalized emission spectral density ($F_{Yb}(\lambda)$) in **1** and the Er^{3+} absorption cross-section at 980 nm ($\sigma_{Er}(\lambda)$) in **3**.

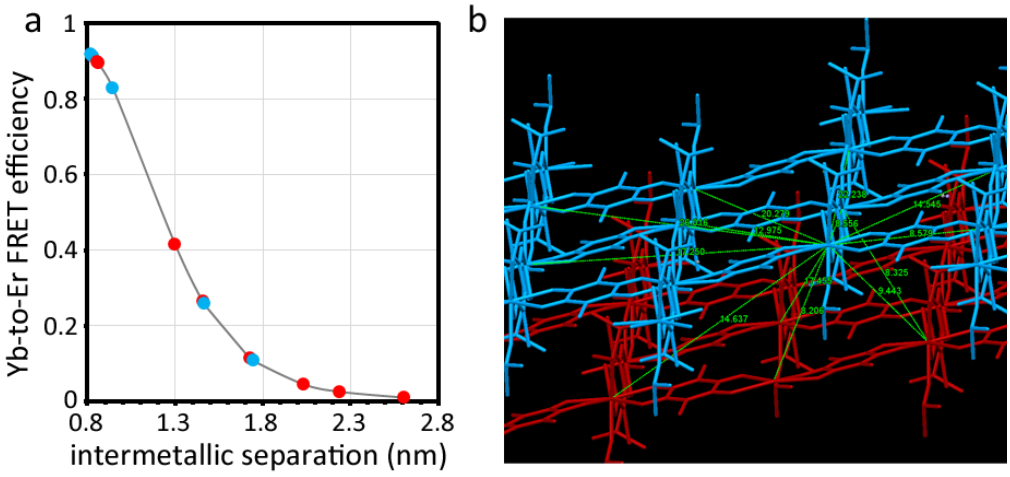

Figure S15. Variation of the efficiency of Yb-to-Er Förster's Resonance Energy Transfer (FRET) on dependence of the intermetallic separation (a) as retrieved from structural data (b). Red and blue dots represent intra- and inter-layer intermetallic distances, respectively.

Thermal analysis

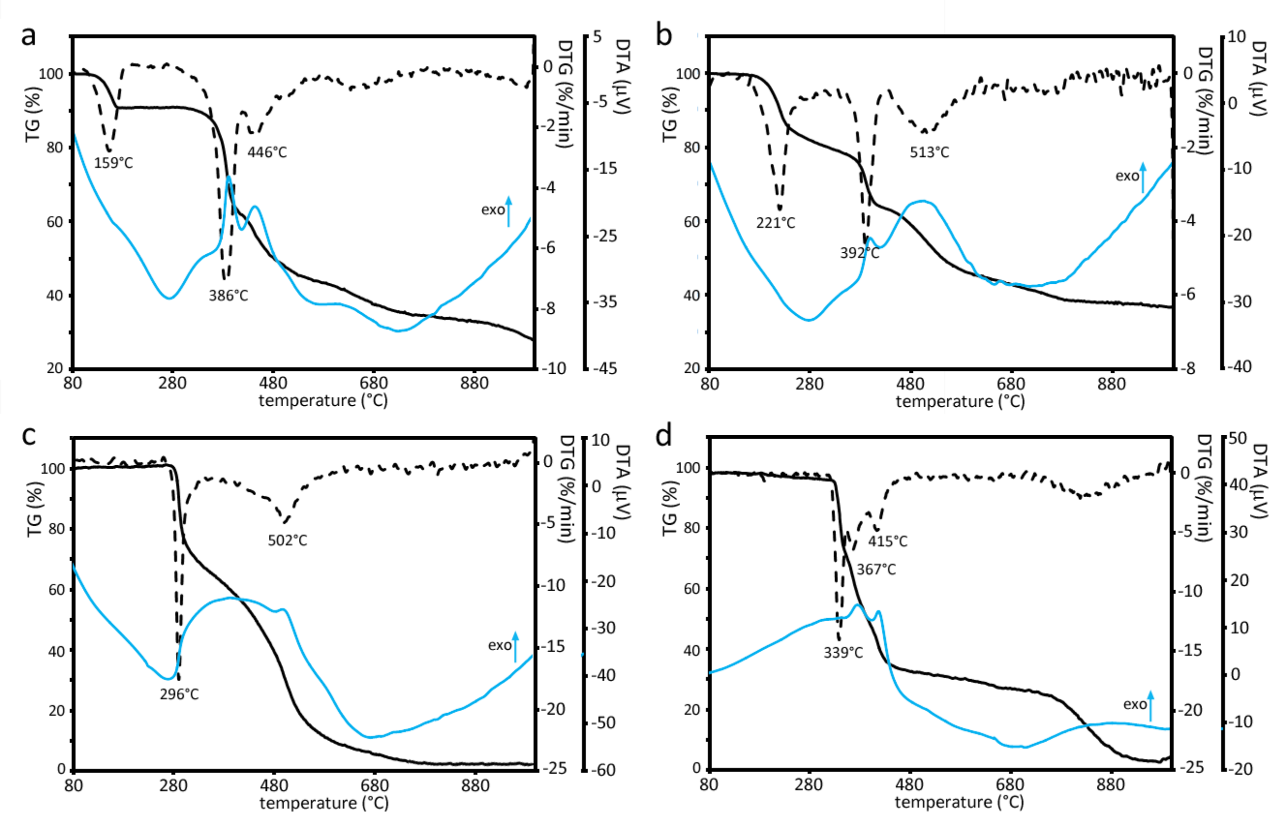

Figure S16. Thermogravigrams (TG, black solid lines), differential thermogravigrams (DTG, back dashed lines) and differential thermal analysis curves (DTA, blue solid lines) of **1** (a), **3** (b), $[(n\text{-Bu})_4N]_3[Al(ClCNAn)_3]$ (c) and KHClCNA (d).

TG, DTG and DTA curves for **1** and **3** (Figures S15a and b) show a similar pattern with an initial mass loss (apparently endothermic) at 159°C and 221°C, respectively, attributed to the loss of 1 or 3 DMSO molecules, followed by an abrupt weight drop, accompanied by exothermic peaks in the DTA curve, likely due to the incipient decomposition of the $ClCNAn^{2-}$ ligands at ~390°C. Complete formation of lanthanide oxide residuals Ln_2O_3 is observed above 800°C. The trend observed in the TG, DTG and DTA curves of the reference $[(n\text{-Bu})_4N]_3[Al(ClCNAn)_3]$ complex and the free KHClCNAn ligand (Figures S15 c and d, respectively), corroborates these attributions. For the Al^{3+} complex derivative, an initial endothermic decomposition of the tetrabutylammonium counterion is observed at 296°C followed by a smooth weight loss (DTG 502°C) due to ligand decomposition, whereas the free KHClCNA starts decomposing at 339°C.

Dropcasted films

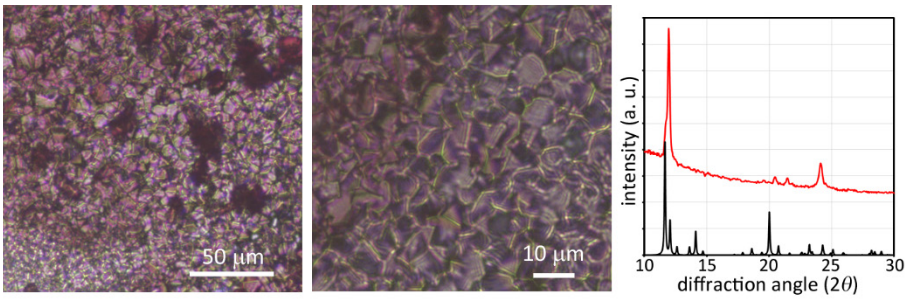

Figure S17. Left: optical microscope images of dropcasted films of **3** at different magnifications. Right: pXRD pattern for a dropcasted film of **3** (red) compared to that simulated from single crystal data (black). Notably, the pattern of the film is dominated by the peaks attributed to the [002] (12.05°) and the [004] (24.10°) diffraction planes, indicating the retention of the crystalline preferential orientation on surface as observed in bulk crystals (Figure S2). Unfortunately, no recognizable pXRD pattern has been retrieved for dropcasted films of **1** and **2** due to the low signal-to-noise ratio. Optical microscope images and pXRD pattern courtesy of Prof. Andrea Falqui and Dr. Danilo Loche at King Abdullah University of Science and Technology (KAUST), Saudi Arabia.

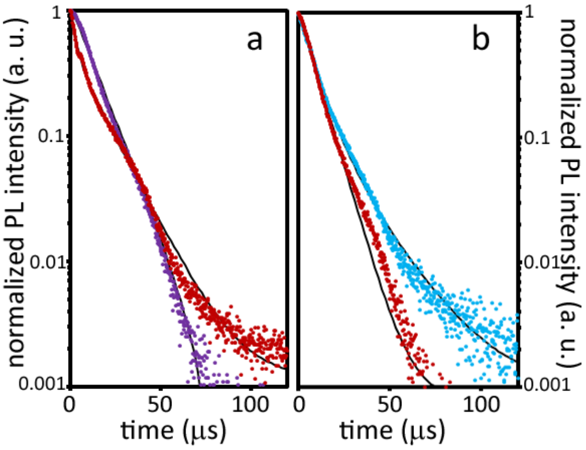

Figure S18. NIR decay dynamics under 470 nm excitation of dropcasted films of **1-3**. a) Yb^{3+} emission at 980 nm in **1** (purple dots) and **2** (red dots) and b) Er^{3+} emission at 1530 nm in **3** (blue dots) and **2** (red dots). Black solid lines represent the best fit to data.

References

S1. M. Atzori, F. Artizzu, *Functional Molecular Materials: An Introductory Textbook*, Pan Stanford Publishing, **2018**

S2. F. Artizzu, F. Quochi, L. Marchiò, E. Sessini, M. Saba, A. Serpe, A. Mura, M. L. M., G. Bongiovanni, P. Deplano, Fully Efficient Direct Yb-to-Er Energy Transfer at Molecular Level in a Near-Infrared Emitting Heterometallic Trinuclear Quinolinolato Complex *J. Phys. Chem. Lett.*, **2013**, *4*, 3062-3066.

S3. S. J. Strickler, R. A. Berg, Relationship between absorption intensity and fluorescence lifetime of molecules. *J. Chem. Phys.*, **1962**, *37*, 814–822.

S4. C. Würth, M. Grabolle, J.a Pauli, M. Spieles, U. Resch-Genger, Relative and absolute determination of fluorescence quantum yields of transparent samples, *Nat. Prot.*, **2013**, *8*, 1535-1550.

S5. F. Artizzu, F. Quochi, M. Saba, L. Marchiò, D. Espa, A. Serpe, A. Mura, M. L. Mercuri, G. Bongiovanni, P. Deplano, Dual Emitting [Yb(5,7ClQ)$_2$(H5,7ClQ)$_2$Cl]: Chemical and Photophysical Properties, *ChemPLUSChem,* **2012**, 77, 240-248.

S6. F. Quochi, F. Artizzu, M. Saba, F. Cordella, M. L. Mercuri, P. Deplano, M. A. Loi, A. Mura, G. Bongiovanni, Population saturation in trivalent erbium sensitized by organic molecular antennae, *J. Phys. Chem. Lett.*, **2010**, *1*, 141–144.

S7. T. Förster, Transfer Mechanism of Electronic Excitation. *Discuss. Faraday Soc.*, **1959**, *27*, 7–17